Atomic and molecular hydrogen in hybrid perovskite solar cells

Yuhang Liang[1], Xiangyuan Cui[2,*], Catherine Stampfl[1], Simon P. Ringer[2], Rongkun Zheng[1,*]

[1] School of Physics, The University of Sydney, NSW 2006, Australia

[2] School of Aerospace, Mechanical and Mechatronic Engineering, The University of Sydney, NSW 2006, Australia

Abstract

Porous organic-inorganic hybrid perovskites are expected to be susceptible to hydrogen. Surprisingly, the roles of hydrogen and the underlying mechanism in perovskites remain poorly understood. Here we present a systematic first-principles study of the stability, electronic properties, and diffusivity of atomic and molecular hydrogen in $MAPbI_3$ and $MASnI_3$. Whereas molecular hydrogen, H_2, is chemically inert, atomic hydrogen, H_i, serves as an electrically active negative-U center, with the calculated U values being -0.85 eV and -1.45 eV for $MAPbI_3$ and $MASnI_3$, respectively. The mobility of atomic H_i is strongly dependent on the charge states. In *p*-type $MAPbI_3$, the H_i^+ proton is the major defect of hydrogen and acts as a source of fast migration, contributing to ionic conductivity and device polarization. Such a behavior is effectively suppressed by *n*-type doping, under which H_2 is dominant. In contrast, H_2 is the lowest-energy hydrogen defect over the whole range of the Fermi energy in $MASnI_3$. The high concentration and low kinetic barriers of H_2 in $MASnI_3$ and *n*-type $MAPbI_3$ suggest the possibility of diffusive hydrogen gas in perovskite solar cells. These findings advance our understanding of how interstitial hydrogen influences hybrid perovskites, providing useful information for the development of perovskite solar cells with improved stability and performance.

Keywords: density functional theory calculation, hydrogen defect, perovskite solar cell materials, formation energy, transition energy levels, ion diffusivity

Introduction

The superb optoelectronic properties, yet low cost, make hybrid halide perovskites emerge as the most compelling candidate for third-generation photovoltaic materials and other electronic devices[1–4]. So far, it has undergone unprecedented progress in power conversion efficiency (PCE) of the single-junction device, from 3.8% in 2009[5] to a recent laboratory-scale 25.6%[6], approaching the state-of-art crystalline-*Si* solar cells (26.6%)[7]. Moreover, for the tandem solar cells with silicon, the PCE has reached 29.15%[8]. Nevertheless, structural defects are of critical importance in hybrid perovskites grown by low-cost techniques. In particular, point defects, both intrinsic and extrinsic, are often chemically active and would intimately affect the carrier diffusion length, recombination rate[9], and consequently the solar cell stability and PCE. Moreover, these ionized species often experience fast ion migration[10–13], especially under irradiation[14], responsible for many electrical anomalies in the operational solar cells, such as the rate-dependent hysteresis in current-voltage curves[15–17].

One of the most significant driving forces behind the success of Methylammonium lead triiodide $MAPbI_3$ ($MA=CH_3NH_3$) lies in its high defect tolerance, with the majority of its intrinsic defects only producing shallow energy levels located close to the conduction band minimum (CBM) or valence band maximum (VBM)[18]. As such, $MAPbI_3$ exhibits exceptional semiconductor characteristics, such as outstanding photoabsorption properties[19] and a long carrier diffusion length[20]. In contrast, its Sn-based counterpart, $MASnI_3$, a promising alternative for solving the toxicity of Pb, lacks these properties[21]. The dominant acceptor V_{Sn} causes unipolar p-type conductivity with high hole densities in $MASnI_3$, and serves as the main underlying mechanism contributing to the reduced PCE [22]. In addition, external metal impurities induced by the electrodes, such as the commonly used Au, also contribute to device degradation[10,23].

As the most abundant element in the universe, hydrogen, serves as another source of external contamination for hybrid perovskites. Hydrogen is ubiquitous during the growth of perovskite films using techniques such as solution process[24] and chemical vapor deposition[25], and from moisture for the operational solar cells. Even for the capsulated devices, the deprotonation of the organic hole transport material, such as Spiro-OMeTAD [2,2',7,7'-tetrakis(N,N-di-p-methoxyphenylamine)-9,9'-

spirobifluorene][2], and the organic cations of hybrid perovskites, can serve as unavoidable sources for hydrogen defects. Owing to its chemical activity and high mobility, hydrogen-in-semiconductor has been a recurrent topic for the semiconductor development[26]. There is experimental evidence of a high-density of hydrogen in perovskites[27–30], but theoretical investigations have been limited to proton diffusion in $MAPbI_3$[31]. The bipolar nature (p-type/n-type)[32] of the host material is expected to influence the ionization states for the defects. However, the relative stability of hydrogen species for different charged states has rarely been studied yet. In addition, due to the porosity of the hybrid halide perovskite lattice, molecular hydrogen H_2 may present and serve as a defect, as found in GaAs[33]. These unintentional defects may have a profound impact on hybrid perovskite solar cells by introducing a source of fast ion diffusion, causing device polarization, compensating built-in electric field, and creating a shunt path, etc. To fully identify the behavior of hydrogen impurities and their effect on the stability and performance of the devices, it is essential to understand the atomic and electronic structures, thermodynamic stability, and kinetic properties.

In this study, we presented an extensive theoretical study of the underlying mechanism of hydrogen-induced impurities in $MAPbI_3$ and $MASnI_3$. Our results show that interstitial hydrogen is likely to be present be both in the atomic (H_i) and molecular (H_2) forms in hybrid perovskites. In particular, in p-type $MAPbI_3$, H_i^+ is the dominant interstitial hydrogen. It acts not only as a donor, but also as an atomic source for fast ion diffusion, contributing to the high ionic conductivity in perovskite solar cells. H_2 is electrically inactive and can occur in high concentrations in $MASnI_3$ and n-type $MAPbI_3$ with high mobility. Moreover, the alignment of atomic hydrogen transition energy levels with respect to the vacuum level implies a useful reference for the study in perovskite solar cells.

Computational method

All the calculations were performed using density functional theory (DFT) as implemented in the Vienna *ab initio* simulation package (VASP)[34]. The projected-augmented wave[35] pseudopotentials were used for describing the ions-electrons interaction and the cutoff energy of the plane basis set employed was 400 eV. A 2 × 2 × 2 reciprocal space K-point mesh was adopted. $MAPbI_3$ has an orthorhombic

(Pnma)[36] crystal structure and $MASnI_3$ has a pseudocubic (P4mm)[37] crystal structure. A 3 × 3 × 3 supercell was employed, resulting in 432 and 324 atoms, respectively for $MAPbI_3$ and $MASnI_3$, respectively, where the atomic positions were fully relaxed until the residual forces were less than 0.01 eV/Å. We compared various van der Waals (vdW) correction methods (**Note 1**, **Table S1 S2**) and adopted the Tkatchenko-Scheffler (TS) scheme[38].

The Perdew-Burke-Ernzerhof (PBE)[39] form of the generalized gradient approximation (GGA) was employed for describing the exchange and correlation functional. The obtained the bandgap values are 1.51 eV and 0.76 eV for $MAPbI_3$ and $MASnI_3$, respectively, compared with experimental values of 1.61 eV[40] and 1.30 eV[41]. For providing a more accurate description of the bandgap, which is underestimated in PBE, the Heyd-Scuseria-Ernzerhof (HSE06)[42] hybrid functional with spin-orbit coupling was also used. In this case, the obtained bandgaps are 1.62 eV for $MAPbI_3$ and 1.28 eV for $MASnI_3$, which are in close agreement with experiment. In this work, we employed both PBE and HSE+SOC to determine defect formation energies and transition energy levels, and used PBE to study the diffusion of hydrogen, as used in $MAPbI_3$[11] and other materials[43].

For an interstitial hydrogen impurity ionized the charge state q, its formation energy $\Delta H_f(H_i^q)$ is calculated by[44]:

$$\Delta H_f(H_i^q) = E(H_i^q) - E(host) - \sum n_i \mu_H + q(E_f + E(VBM) + \Delta V) \quad (1)$$

where $E(H_i^q)$ and $E(host)$ are the ground state total energies of impurity-containing and pristine systems, respectively. n_i is the number of hydrogen atoms incorporated into the system, and μ_H is the chemical potential of hydrogen which was set to the half of total energy of a H_2 molecule. $E(VBM)$ represents the energy of the valance band maximum (VBM) of the host, and E_f is the Fermi energy with respect to the VBM. The correction term, ΔV, is used for ensuring the alignment of potential for the charged defect in supercells.

By using the calculated formation energy ΔH_f, we can estimate the concentration of defect species in thermal equilibrium by[44]:

$$N = N_0 e^{-\frac{\Delta H_f}{k_B T}} \quad (2)$$

Here, N_0 is the number of the defect species per volume. k_B is the Boltzmann constant and T represents temperature, which was set to room temperature ($T = 300K$).

The transition energy level $\mathcal{E}(q/q')$ is the Fermi level position for which the formation energy of H_i^q is equal to that of $H_i^{q'}$, thus, can be determined by[44]:

$$\mathcal{E}(q/q') = [E(a,q) - E(a,q') - (q-q')(E(VBM) + \Delta V)]/(q-q') \quad (3)$$

The hydrogen impurity diffusion pathway and its diffusion energy profile were calculated by the nudged elastic band (NEB) method in conjunction with the climbing image method[45–47], as implemented using the VASP Transition State Tool. For each species, six images are linearly incorporated between the initial and final states of relaxed structures.

Results and discussions

The calculated formation energy of interstitial hydrogen in $MAPbI_3$ as a function of the Fermi energy (E_f) is shown in **Figure 1a**. While the trends are similar, the formation energies calculated by PBE (red) are ~ 0.2 eV above those by HSE+SOC (green) for the whole range of the E_f. Atomic hydrogen H_i is amphoteric – it can act as both a donor (H_i^+) or an acceptor (H_i^-). The neutrally charged state H_i^0 is not thermodynamically stable over the whole range of the Fermi level. Under *p*-type conditions, in which the E_f is close to the VBM, the positively charged state of H_i^+ is stable, while under *n*-type conditions with E_f approaching to the CBM, the negatively charged state of H_i^- has the lower formation energy. Based on PBE (HSE+SOC) functionals, the charge transition level $\varepsilon(0/+)$ occurs at 0.12 (0.08) eV above the CBM, and the charge transition level $\varepsilon(0/-)$ is 0.55 (0.77) eV below the CBM. The energy difference between the $\varepsilon(0/+)$ and $\varepsilon(0/-)$ transition levels lead to a negative U value of –0.67 (-0.85) eV. In this case, $\varepsilon(+/-)$ become an effective transition energy level for H_i in $MAPbI_3$, i.e., the crossing point in **Figure 1a**, with the value of 1.30 (1.26) eV above the VBM based on the PBE (HSE+SOC) functional.

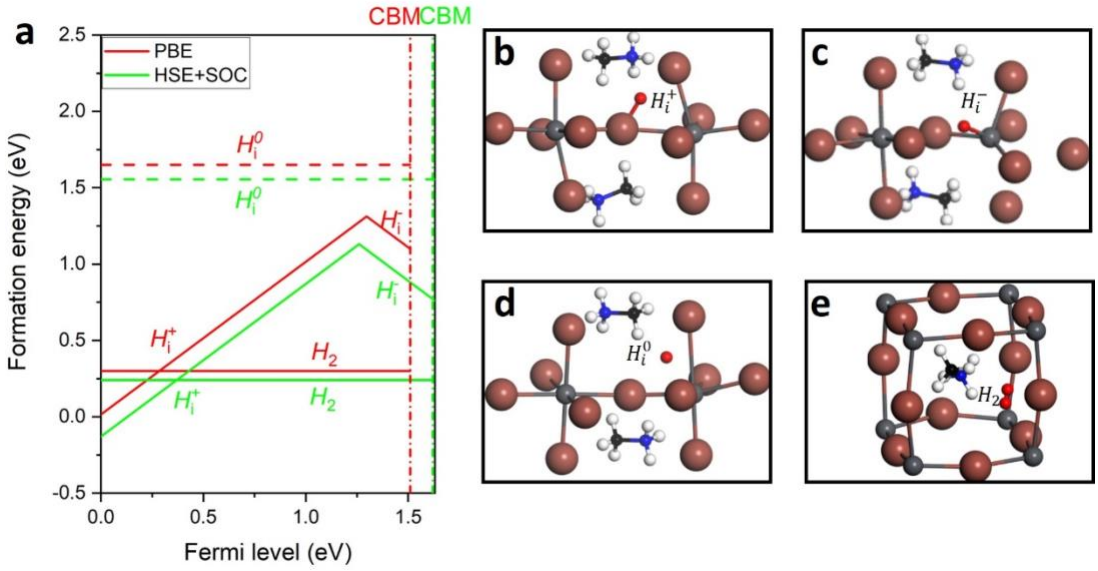

Figure 1. (**a**) Calculated formation energy versus Fermi level, E_f, of the interstitial hydrogen impurity in $MAPbI_3$, using PBE (red) and HSE+SOC (green). The short dash dot lines represent the positions of conduction band maximum (CBM). The atomic structures of the lowest energy interstitial hydrogen (**b**) H_i^+, (**c**) H_i^-, (**d**) H_i^0, and (**e**) H_2 in $MAPbI_3$. I atoms are depicted as brown spheres, Pb in grey, C in black, N in blue, host H in white, and the hydrogen impurities are highlighted in red.

The negative-U feature has been found in many technologically significant semiconductors[48], serving as a characteristic to analyze the interaction between atomic hydrogen and host. In $MAPbI_3$, it originates from the strong dependence of H_i atomic sites on its ionization states. After comparing various configurations including defect position at $Pb-I$ bond-centers, Pb (I) antibonding sites, and lattice void sites, positively charged H_i^+ prefers to reside next to the host I anions by forming a $H-I$ bond with a bond length of 1.42 Å, as shown in **Figure 1b**. Two nearby I anions are moved inward to H_i^+, and the bond is aligned toward another neighboring I anion. Such a preference for the antibonding site is in stark contrast to that in ZnO[49] and GaAs[33], in which bond-center sites are energetically most stable for H_i^+. This can be attributed to the high ionic character of halide perovskite materials[50]. Similarly, negatively charged H_i^- tends to bind to cation Pb^{2+} with a bond length of 1.66 Å, as shown in **Figure 1c**. The H-bonded Pb cation is largely displaced toward the impurity center by

about 1.3 Å from the original position, while the neighbouring I anions move outward, resulting in the evident structural distortion of the PbI_6 octahedron. In comparison, the essentially unstable neutral-charged H_i^0 prefers to be located in between those of H_i^+ and H_i^-, thus being situated at the void center of the triangular region formed between three adjacent I^- ions, as shown in **Figure 1d**. The distances between H_i^0 and the nearby host atoms are evaluated to be more than 2.50 Å, so the chemically inert H_i^0 is more like an isolated species with regard to the surrounding host ions. These distinct hydrogen positioning preferences in general agree with the previous study[31].

Significantly, interstitial hydrogen can exist in the molecular form neutral H_2, acting as an electrically inactive agent over the whole range of E_f of $MAPbI_3$. The energetically most favourable configuration is shown in **Figure 1e**, for which H_2 is positioned stably occupies in the center between the adjacent ions corresponding to the largest void region. The corresponding molecular bond length of H_2 is 0.78 Å, compared with 0.75 Å of free H_2 . The distances between each H of the molecule and the nearby host atoms are all greater than 3.00 Å, confirming the chemical inertness of H_2 with the host. Significantly, from **Figure 1a**, for p-type $MAPbI_3$, atomic H_i^+ is the major interstitial hydrogen due to the lowest formation energy. In n-type $MAPbI_3$, molecular H_2 becomes the dominant interstitial hydrogen with a concentration estimated to be $-1.16 \times 10^{16} cm^{-3}$ at 300K, based on the HSE+SOC value.

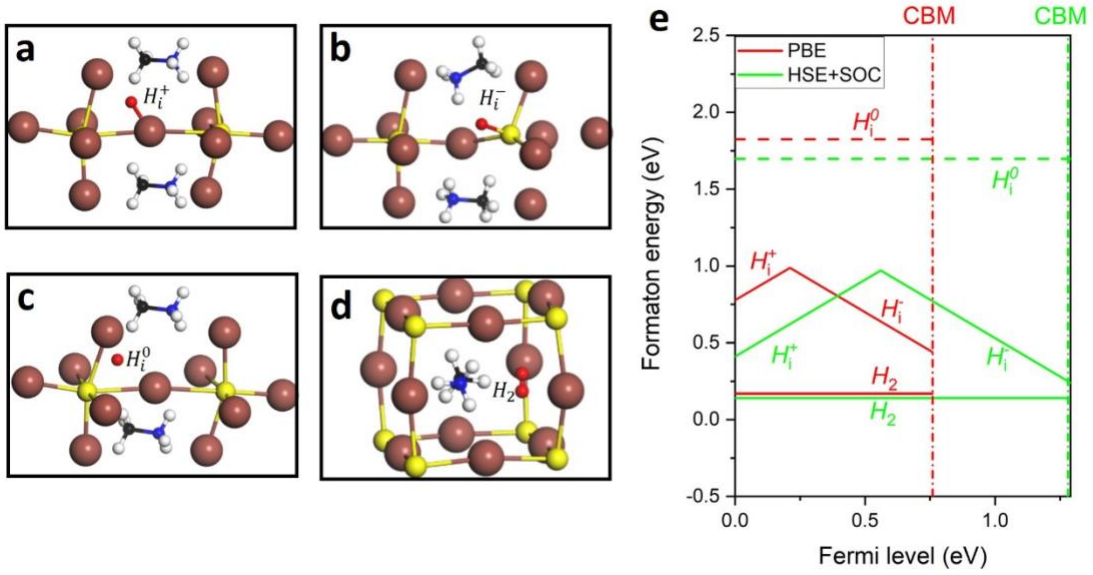

Figure 2. The atomic structures of the host with a (**a**) H_i^+, (**b**) H_i^-, (**c**) H_i^0, and (**d**) H_2 in $MASnI_3$. (**e**) Calculated formation energy of interstitial hydrogen in $MASnI_3$ for different defect states as a function of the Fermi energy, E_f. I atoms are depicted as brown spheres, Sn in yellow, C in black, N in blue, host H in white, and the hydrogen impurities are highlighted in red.

For $MASnI_3$, the local geometries of the energetically favourable interstitial hydrogen, including atomic and molecular hydrogens (H_i, H_2), are very similar to those in $MAPbI_3$, as shown in **Figure 2a-d**. The $H-I$ bond for H_i^+ exhibits the same bond length of 1.42 Å as that in $MAPbI_3$. For H_i^- state, $H-Sn$ exhibits a shorter chemical bond of 1.53 Å than the $H-Pb$ bond of 1.66 Å in $MAPbI_3$. The lowest energy H_2 in $MASnI_3$ is also located at the largest void region, with a bond length of 0.76 Å. Despite the similarity of the atomic structures of hydrogen, the corresponding energetics are distinctively different between $MAPbI_3$ and $MASnI_3$. The calculated hydrogen formation energy for the different states in $MASnI_3$ is plotted in **Figure 2e**. Neutral molecular H_2 has the lowest formation energy over the whole range of the Fermi level, E_f. Thus, unlike $MAPbI_3$, molecular H_2 acts as the dominant form of hydrogen in both *p*- and *n*-type $MASnI_3$. The calculated formation energies of H_2 from PBE and HSE+SOC functionals are 0.17 eV and 0.14 eV, respectively. The corresponding equilibrium concentration of H_2 in $MASnI_3$ is $\sim 1.05 \times 10^{18} cm^{-3}$ at 300K. For atomic hydrogen, it is also electrically active and forms as a negative-U center in $MASnI_3$, like in $MAPbI_3$. H_i^+ and H_i^- display a lower formation energy than H_i^0. The greater bandgap variation in $MASnI_3$ between PBE and HSE+SOC leads to a larger deviation of the $(+/-)$ transition energy level, compared to $MAPbI_3$. The HSE+SOC transition level, $\varepsilon(+/-)$, is located at 0.56 eV above VBM. Moreover, from the $\varepsilon(0/+)$ and $\varepsilon(0/-)$ energy positions, the U value for $MASnI_3$ is calculated to be -1.45 eV, which is more negative than that of $MAPbI_3$, indicating a stronger ionic character in $MASnI_3$[51].

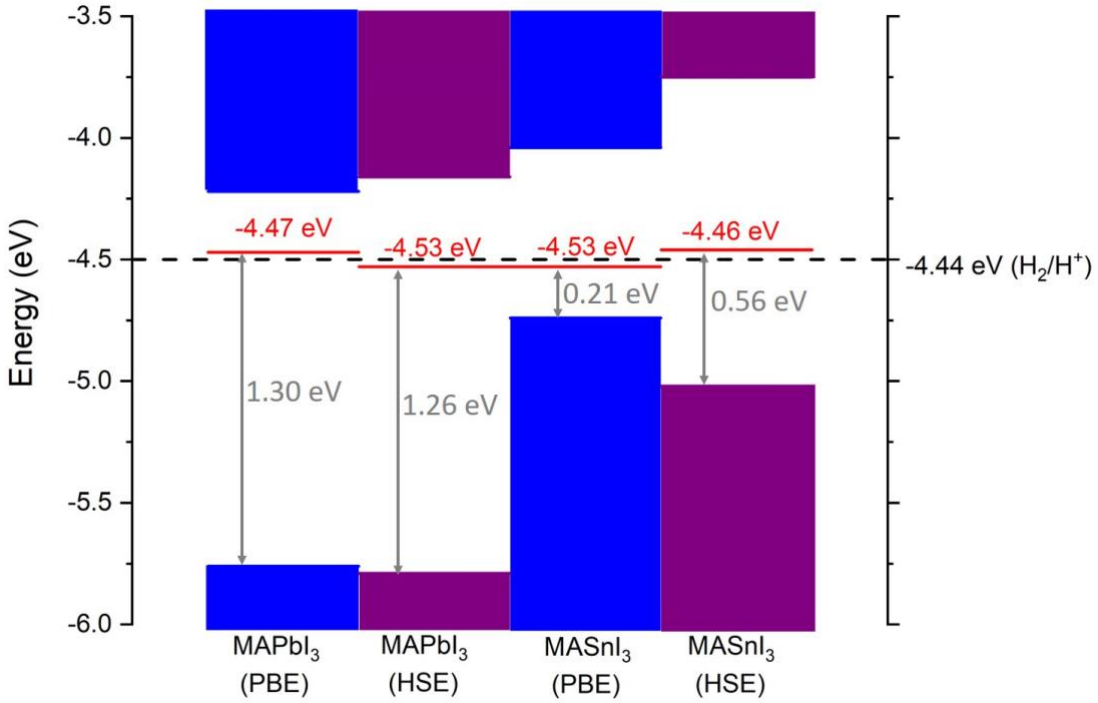

Figure 3. The absolute energy position of the transition energy level $\varepsilon(+/-)$ of atomic hydrogen and the band edge of $MAPbI_3$ and $MASnI_3$, based on PBE and HSE+SOC calculations, where the vacuum level was set to zero. The dashed line is labelled for the chemical potential of the standard hydrogen electrode (SHE).

Figure 3 shows the transition energy levels $\varepsilon(+/-)$ of atomic H_i with respect to the VBM in $MAPbI_3$ and $MASnI_3$ obtained with the PBE and HSE+SOC. The bands are aligned on an absolute energy scale through the identification of the vacuum level[52,53], in which the I-1s core level was taken as the reference. The transition level of $\varepsilon(+/-)$ exhibits a remarkable consistency, i.e., ~-4.4 eV below the vacuum level with a variation less than 0.1 eV, for both systems with different functionals. This feature is in fine agreement with the universal alignment of hydrogen $(+/-)$ levels predicted using local density approximation functional[48]. The similarity of transition levels in terms of different exchange-correlation functionals can be attributed to the identical description in energy difference for the charge localized defect[53]. It is noted that such a transition energy level $\varepsilon(+/-)$ of H_i, ~4.44 eV below the vacuum level, also corresponds to the

absolute energy of the standard water redox potential, namely the chemical potential of the standard hydrogen electrode[54]. This alignment of hydrogen levels $\varepsilon(+/-)$ thus provides a potential reference level for the study of hybrid perovskite photovoltaics.

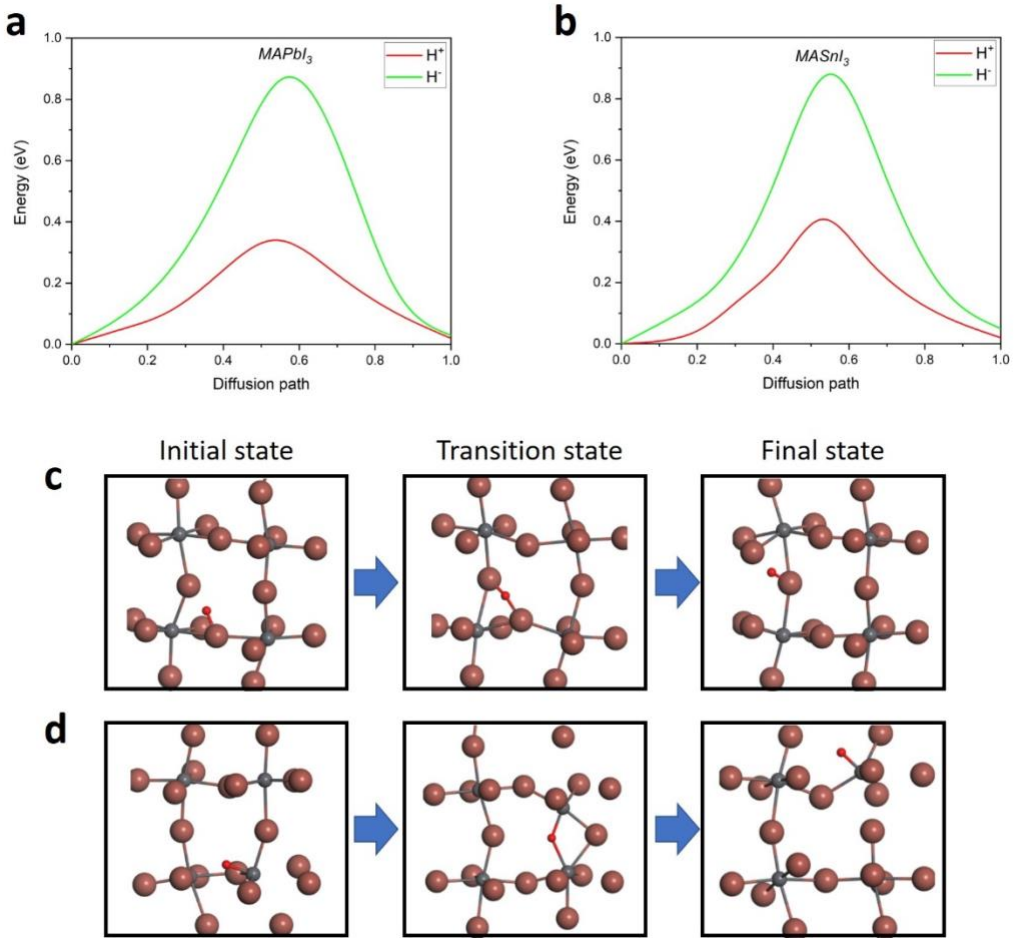

Figure 4. The calculated diffusion energy profiles of H_i^+ (red) and H_i^-(green) in (**a**) $MAPbI_3$ and (**b**) $MASnI_3$. The atomic structures of the initial, the transition, and the final states for the migration of (**c**) H_i^+ and (**d**) H_i^- in $MAPbI_3$. For representing each atom, I-brown, Pb-grey, and H impurity-red.

Halide perovskites are well-known mixed electronic/ionic conductors, in which the ionic conductivity is comparable to the electronic one[13]. The ion migration is associated with the high-density charged defects in the crystal, resulting in many anomalies in photovoltaic applications. As in diverse traditional semiconductors[55–58],

the diffusion of hydrogen species could be a common cause of ionic conductivity in hybrid perovskites. Therefore, having discussed the thermodynamic stability of hydrogen, we next examine the mobility of interstitial hydrogen.

Figure 4a and 4b illustrate the energy profiles along the atomic hydrogen migration in the lattice of $MAPbI_3$ and $MASnI_3$, respectively. The starting point ($x = 0$) is defined as the configuration of the initial state, and the end point ($x = 1$) is the final site during the diffusion. The highest point corresponds to the transition state. As expected[51,59,60], in both materials, the diffusion barriers of H_i^+ are significantly lower than those of H_i^- due to the significantly smaller ionic radius of H_i^+ compared to H_i^-. This feature is different from most of the native defects in hybrid perovskites that have similar energy profiles for different charge states [11], e.g., halide vacancy and organic cation vacancy. As discussed earlier, H_i^+ and H_i^- have different bonding environments and involve distinctive diffusion pathways. As shown in **Figure. 4c**, and **S1a**, the $I^- - I^-$ diffusion of H_i^+ essentially goes through the transition state by forming transient bonds connecting two neighboring I^-. The calculated diffusion barriers are 0.34 eV and 0.41 eV for H_i^+ in $MAPbI_3$ and $MASnI_3$, respectively. The former value is compared with the proton diffusion barrier, 0.29 eV, in $MAPbI_3$ by Egger *et al.*[31] using a smaller 40-atom supercell. In contrast, the diffusion of the much larger H_i^- ion in $MAPbI_3$ undertakes a $Pb^{2+} - Pb^{2+}$ pathway and involves significant structural distortion, as shown in **Figure 4b**. The puckered $Pb - I - Pb$ framework pushes H_i^- hopping forward and finally binding to another Pb cation with the structural recovery. Due to a similar bonding environment, a similar $Sn^{2+} - Sn^{2+}$ diffusion happens to $MASnI_3$, as depicted in **Figure S1b**. These significant lattice distortions correspond to large diffusion barriers, i.e., 0.87 eV and 0.88 eV for H_i^- in $MAPbI_3$ and $MASnI_3$, respectively.

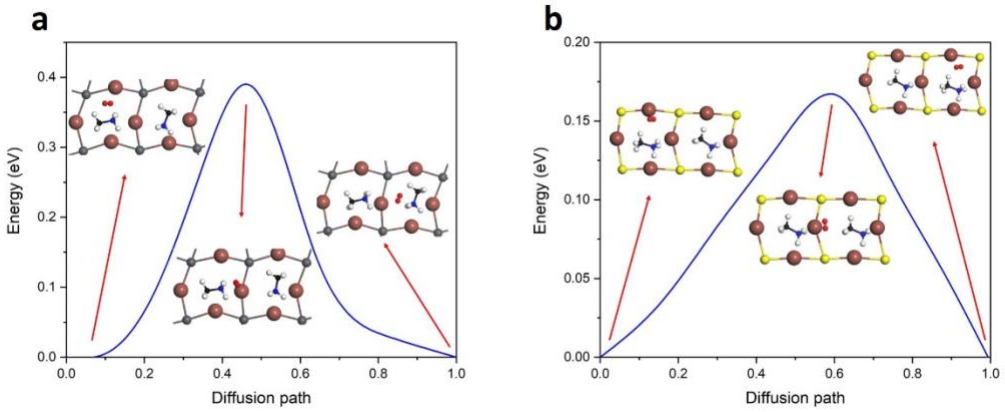

Figure 5 The calculated energy profiles during the migration of H_2 in (**a**) $MAPbI_3$ and (**b**) $MASnI_3$, where the insets are the schematics of the corresponding NEB images.

We have also investigated the kinetic property of molecular hydrogen H_2 in perovskite layers. **Figure 5** illustrates the energy profiles of H_2 diffusion in $MAPbI_3$ and $MASnI_3$. Despite the larger size, H_2 is quite diffusive in both systems, due to its chemical inertness and the structural porosity of the perovskite lattice. The calculated diffusion barrier of H_2 is 0.39 eV in $MAPbI_3$, and 0.17 eV in $MASnI_3$. From the NEB images, the diffusions of H_2 show weak interaction with the host matrix. It can easily migrate between adjacent cavities of the inorganic scaffold along the void across a framework of $Pb_4I_4(Sn_4I_4)$ square planes, accompanied by self-rotation.

We emphasize that the diffusion barrier of 0.34 eV for H_i^+ in *p*-type $MAPbI_3$ is rather low and comparable to those of the main diffusing native defects (0.30 eV for V_I and 0.57 eV for V_{MA})[11]. This suggests that H_i^+ can easily diffuse at room temperature and acts as a primary contributor to the higher ionic conductivity in *p*-type $MAPbI_3$ films and crystals[61,62]. Such a conclusion also provides theoretical evidence for the recent experimental observations of fast proton diffusion[27–30]. Moreover, under the photo-generated built-in electric field, the charged species will be driven to the selective contact and cause accumulation near the interfaces, among which the high concentration H_i^+ would cause a much more significant field-screening effect through faster process than most native defects[11]. As a result, the charge carrier separation and collection of the device will be influenced, leading to the polarization and degradation of the device performance. The photocurrent density changes with respect to the

redistribution process, so as to influence the current-voltage measurements in perovskite solar cells and could be subject to under- or over-estimate of the device performance.

When fabricated for *n*-type $MAPbI_3$, e.g., grown by I-poor/Pb-rich condition[18], electrically inactive H_2 becomes the dominant defect for interstitial hydrogen. Thus, ion diffusion of the proton will be effectively suppressed in *n*-type $MAPbI_3$, further improving solar cell performance stability. H_2 is the main interstitial hydrogen in $MASnI_3$, under both *p*- and *n*-type conditions. Unlike H_i, H_2 is not driven by the built-in electric field or applied bias, though it also has a relatively low diffusion barrier and high density in both *n*-doped $MAPbI_3$ and $MASnI_3$.

Conclusion

Based on extensive first-principles DFT calculations, we systematically investigated hydrogen as the interstitial defects in hybrid perovskites and their roles in solar cells. In both $MAPbI_3$ and $MASnI_3$, molecular hydrogen H_2 is electrically inert exhibiting a weak interaction with the hosts. By contrast, atomic hydrogen H_i is chemically active and shows a typical negative-U behavior with the transition energy levels $\varepsilon(+/-)$ located at around 4.44 eV below the vacuum level. H_2 is the major hydrogen defect in $MASnI_3$ and *n*-type $MAPbI_3$. The low kinetic barriers suggest the possibility of highly diffusive hydrogen gas in perovskite absorbers of solar cells. For *p*-type $MAPbI_3$, H_i^+ is dominant and involve a fast ion diffusion, serving as an atomic source for ionic conductivity observed in current solar cells. Furthermore, such a charged species would cause ionic accumulation at contact or interface, leading to device polarization and a photogenerated field-screening effect.

Acknowledgements

We acknowledge the expert support provided by the Sydney Informatics Hub (SIH) team—a core research facility of the University of Sydney. This work was supported by computational resources provided by the Australian Government through Gadi under the National Computational Merit Allocation Scheme and was partially accessed

through the SIH HPC Allocation Scheme. SPR acknowledges partial financial support from the Australian Research Council [DP200100940].

Reference

[1] G. Grancini, M. K. Nazeeruddin, *Nature Reviews Materials* **2019**, *4*, 4.
[2] M. Jeong, I. W. Choi, E. M. Go, Y. Cho, M. Kim, B. Lee, S. Jeong, Y. Jo, H. W. Choi, J. Lee, J.-H. Bae, S. K. Kwak, D. S. Kim, C. Yang, *Science* **2020**, *369*, 1615.
[3] Y. Liang, F. Li, R. Zheng, *Adv. Electron. Mater.* **2020**, 2000137.
[4] J. Huang, Y. Yuan, Y. Shao, Y. Yan, *Nature Reviews Materials* **2017**, *2*, 1.
[5] A. Kojima, K. Teshima, Y. Shirai, T. Miyasaka, *J. Am. Chem. Soc.* **2009**, *131*, 6050.
[6] J. Jeong, M. Kim, J. Seo, H. Lu, P. Ahlawat, A. Mishra, Y. Yang, M. A. Hope, F. T. Eickemeyer, M. Kim, Y. J. Yoon, I. W. Choi, B. P. Darwich, S. J. Choi, Y. Jo, J. H. Lee, B. Walker, S. M. Zakeeruddin, L. Emsley, U. Rothlisberger, A. Hagfeldt, D. S. Kim, M. Grätzel, J. Y. Kim, *Nature* **2021**, 1.
[7] L. Meng, J. You, Y. Yang, *Nat Commun* **2018**, *9*, 5265.
[8] A. Al-Ashouri, E. Köhnen, B. Li, A. Magomedov, H. Hempel, P. Caprioglio, J. A. Márquez, A. B. M. Vilches, E. Kasparavicius, J. A. Smith, N. Phung, D. Menzel, M. Grischek, L. Kegelmann, D. Skroblin, C. Gollwitzer, T. Malinauskas, M. Jo, R. Schlatmann, M. Topic, L. Korte, A. Abate, B. Stannowski, D. Neher, M. Stolterfoht, T. Unold, V. Getautis, S. Albrecht, *Science* **2020**, *370*, 1300.
[9] Y. Chen, H. Zhou, *Journal of Applied Physics* **2020**, *128*, 060903.
[10] W. Ming, D. Yang, T. Li, L. Zhang, M.-H. Du, *Adv. Sci.* **2018**, *5*, 1700662.
[11] J. Haruyama, K. Sodeyama, L. Han, Y. Tateyama, *J. Am. Chem. Soc.* **2015**, *137*, 10048.
[12] J. M. Azpiroz, E. Mosconi, J. Bisquert, F. De Angelis, *Energy Environ. Sci.* **2015**, *8*, 2118.
[13] T.-Y. Yang, G. Gregori, N. Pellet, M. Grätzel, J. Maier, *Angewandte Chemie* **2015**, *54*, 7905.
[14] J. T. DuBose, P. V. Kamat, *J. Am. Chem. Soc.* **2020**, *142*, 5362.
[15] B. C. O'Regan, P. R. F. Barnes, X. Li, C. Law, E. Palomares, J. M. Marin-Beloqui, *J. Am. Chem. Soc.* **2015**, *137*, 5087.
[16] S. Meloni, T. Moehl, W. Tress, M. Franckevičius, M. Saliba, Y. H. Lee, P. Gao, M. K. Nazeeruddin, S. M. Zakeeruddin, U. Rothlisberger, M. Graetzel, *Nat Commun* **2016**, *7*, 10334.
[17] Z. Xiao, Y. Yuan, Y. Shao, Q. Wang, Q. Dong, C. Bi, P. Sharma, A. Gruverman, J. Huang, *Nature Mater* **2015**, *14*, 193.
[18] W.-J. Yin, T. Shi, Y. Yan, *Appl. Phys. Lett.* **2014**, *104*, 063903.
[19] A. M. A. Leguy, P. Azarhoosh, M. I. Alonso, M. Campoy-Quiles, O. J. Weber, J. Yao, D. Bryant, M. T. Weller, J. Nelson, A. Walsh, M. van Schilfgaarde, P. R. F. Barnes, *Nanoscale* **2016**, *8*, 6317.
[20] Q. Dong, Y. Fang, Y. Shao, P. Mulligan, J. Qiu, L. Cao, J. Huang, *Science* **2015**, *347*, 967.
[21] T. Shi, H.-S. Zhang, W. Meng, Q. Teng, M. Liu, X. Yang, Y. Yan, H.-L. Yip, Y.-J. Zhao, *J. Mater. Chem. A* **2017**, *5*, 15124.
[22] Z. Shi, J. Guo, Y. Chen, Q. Li, Y. Pan, H. Zhang, Y. Xia, W. Huang, *Adv. Mater.* **2017**, *29*, 1605005.
[23] K. Domanski, J.-P. Correa-Baena, N. Mine, M. K. Nazeeruddin, A. Abate, M. Saliba,

W. Tress, A. Hagfeldt, M. Grätzel, *ACS Nano* **2016**, *10*, 6306.
[24] Y. Chen, M. He, J. Peng, Y. Sun, Z. Liang, *Advanced Science* **2016**, *3*, 1500392.
[25] C. Mortan, T. Hellmann, M. Buchhorn, M. d'Eril Melzi, O. Clemens, T. Mayer, W. Jaegermann, *Energy Science & Engineering* **2020**, *8*, e734.
[26] C. G. Van de Walle, J. Neugebauer, *Annual Review of Materials Research* **2006**, *36*, 179.
[27] S. Sadhu, T. Buffeteau, S. Sandrez, L. Hirsch, D. M. Bassani, *J. Am. Chem. Soc.* **2020**, *142*, 10431.
[28] C. Cardenas-Daw, T. Simon, J. K. Stolarczyk, J. Feldmann, *J. Am. Chem. Soc.* **2017**, *139*, 16462.
[29] D. R. Ceratti, A. Zohar, R. Kozlov, H. Dong, G. Uraltsev, O. Girshevitz, I. Pinkas, L. Avram, G. Hodes, D. Cahen, *Advanced Materials* **2020**, *32*, 2002467.
[30] Y.-F. Chen, Y.-T. Tsai, L. Hirsch, D. M. Bassani, *J. Am. Chem. Soc.* **2017**, *139*, 16359.
[31] D. A. Egger, L. Kronik, A. M. Rappe, *Angew. Chem. Int. Ed.* **2015**, *54*, 12437.
[32] L. A. Frolova, N. N. Dremova, P. A. Troshin, *Chem. Commun.* **2015**, *51*, 14917.
[33] L. Pavesi, P. Giannozzi, *Phys. Rev. B* **1992**, *46*, 4621.
[34] G. Kresse, J. Furthmüller, *Computational Materials Science* **1996**, *6*, 15.
[35] G. Kresse, D. Joubert, *Phys. Rev. B* **1999**, *59*, 1758.
[36] M. T. Weller, O. J. Weber, P. F. Henry, A. M. Di Pumpo, T. C. Hansen, *Chem. Commun.* **2015**, *51*, 4180.
[37] E. S. Parrott, R. L. Milot, T. Stergiopoulos, H. J. Snaith, M. B. Johnston, L. M. Herz, *J. Phys. Chem. Lett.* **2016**, *7*, 1321.
[38] A. Tkatchenko, M. Scheffler, *Phys. Rev. Lett.* **2009**, *102*, 073005.
[39] J. P. Perdew, K. Burke, M. Ernzerhof, *Phys. Rev. Lett.* **1996**, *77*, 3865.
[40] Y. Yamada, T. Nakamura, M. Endo, A. Wakamiya, Y. Kanemitsu, *Appl. Phys. Express* **2014**, *7*, 032302.
[41] F. Hao, C. C. Stoumpos, P. Guo, N. Zhou, T. J. Marks, R. P. H. Chang, M. G. Kanatzidis, *J. Am. Chem. Soc.* **2015**, *137*, 11445.
[42] J. Heyd, G. E. Scuseria, M. Ernzerhof, *The Journal of Chemical Physics* **2006**, *124*, 219906.
[43] Y. Liang, X. Cui, F. Li, C. Stampfl, S. P. Ringer, R. Zheng, *Phys. Rev. Materials* **2021**, *5*, 035405.
[44] C. G. Van de Walle, J. Neugebauer, *Journal of Applied Physics* **2004**, *95*, 3851.
[45] G. Henkelman, H. Jónsson, *The Journal of Chemical Physics* **2000**, *113*, 9978.
[46] G. Mills, H. Jónsson, G. K. Schenter, *Surface Science* **1995**, *324*, 305.
[47] G. Henkelman, B. P. Uberuaga, H. Jónsson, *The Journal of Chemical Physics* **2000**, *113*, 9901.
[48] C. G. Van de Walle, J. Neugebauer, *Nature* **2003**, *423*, 626.
[49] C. G. Van de Walle, *Phys. Rev. Lett.* **2000**, *85*, 1012.
[50] J.-W. Lee, N.-G. Park, *Advanced Energy Materials* **2020**, *10*, 1903249.
[51] J. Neugebauer, C. G. Van de Walle, *Phys. Rev. Lett.* **1995**, *75*, 4452.
[52] Y. Hinuma, F. Oba, Y. Kumagai, I. Tanaka, *Phys. Rev. B* **2012**, *86*, 245433.
[53] A. Alkauskas, A. Pasquarello, *Phys. Rev. B* **2011**, *84*, 125206.
[54] S. Trasatti, *Electrochimica Acta* **1987**, *32*, 843.
[55] M. S. Islam, A. M. Nolan, S. Wang, Q. Bai, Y. Mo, *Chem. Mater.* **2020**, *32*, 5028.
[56] Ch. Karmonik, R. Hempelmann, J. Cook, F. Güthoff, *Ionics* **1996**, *2*, 69.
[57] K. D. Kreuer, *Annual Review of Materials Research* **2003**, *33*, 333.
[58] K.-D. Kreuer, S. J. Paddison, E. Spohr, M. Schuster, *Chem. Rev.* **2004**, *104*, 4637.
[59] C. G. Van de Walle, P. J. H. Denteneer, Y. Bar-Yam, S. T. Pantelides, *Phys. Rev. B* **1989**, *39*, 10791.

[60] S. Limpijumnong, C. G. Van de Walle, *Phys. Rev. B* **2003**, *68*, 235203.
[61] Y. Li, C. Li, H. Yu, B. Yuan, F. Xu, H. Wei, B. Cao, *Front. Chem.* **2020**, *8*, 754.
[62] A. Senocrate, I. Moudrakovski, G. Y. Kim, T.-Y. Yang, G. Gregori, M. Grätzel, J. Maier, *Angewandte Chemie International Edition* **2017**, *56*, 7755.